Sister Rod Destructive Examinations (FY22)

Appendix F2: Evaluation of Fuel Rod Fatigue During Spent Fuel Transportation

Spent Fuel and Waste Disposition

Prepared for
US Department of Energy

Spent Fuel and Waste Science and Technology

Oak Ridge National Laboratory

Paul Cantonwine, Rose Montgomery, Hong Wang, Bruce Bevard,

January 13, 2023

M2SF-23OR010201024

ORNL/SPR-2022/2736

SUMMARY

This report documents work performed under the Spent Fuel and Waste Disposition's Spent Fuel and Waste Science and Technology program for the US Department of Energy (DOE) Office of Nuclear Energy (NE). This work was performed to fulfill Level 2 Milestone M2SF-23OR010201024, "FY22 Report on ORNL Sibling Rod Testing Results," within work package SF-23OR01020102 and is an update to the work reported in M2SF-22OR010201047, M2SF-21OR010201032, M2SF-19ORO010201026, and M2SF-19OR010201028.

As a part of DOE NE High Burnup Spent Fuel Data Project, Oak Ridge National Laboratory (ORNL) is performing destructive examinations (DEs) of high burnup (HBU) (>45 GWd/MTU) spent nuclear fuel (SNF) rods from the North Anna Nuclear Power Station operated by Dominion Energy. The SNF rods, called *sister rods* or *sibling rods*, are all HBU and include four different kinds of fuel rod cladding: standard Zircaloy-4 (Zirc-4), low-tin (LT) Zirc-4, ZIRLO, and M5. The DEs are being conducted to obtain a baseline of the HBU rods' condition before dry storage and are focused on understanding overall SNF rod strength and durability. Composite fuel and defueled cladding will be tested to derive material properties. Although the data generated can be used for multiple purposes, one primary goal for obtaining the post-irradiation examination data and the associated measured mechanical properties is to support SNF dry storage licensing and relicensing activities by (1) addressing identified knowledge gaps and (2) enhancing the technical basis for post-storage transportation, handling, and subsequent disposition.

This appendix documents an evaluation of the fatigue data to enhance the technical basis for post-storage transportation, handling, and subsequent disposition and to identify future testing needs for Phase 2 of the project. The following is a summary of the evaluation process, findings, and future plans.

The fatigue evaluation of spent nuclear fuel under transportation conditions is one where the magnitude of the cyclic history is expected to be less than the fatigue limit of the fuel rods. Thus, to conclude fatigue failures do not occur, it is sufficient to show that a strain amplitude representing an expected cyclic history is less than the fatigue or endurance limit of the spent nuclear fuel rods (also defined in terms of strain amplitude). The fatigue evaluation herein considers the current available fatigue test data on cladding materials and high burnup fuel rods, the potential non-conservatisms in the HBU fuel rod test data, and the measured cyclic data reported in the MMTT for defining a conservative bounding strain amplitude to represent the expected cyclic history resulting from normal transportation vibration environments.

The HBU fuel rod fatigue data (tested under zero mean strain conditions) indicate the rod level fatigue limit is degraded compared to cladding alloy only test data. Using the form of the O'Donnell-Langer design curve for Zircaloy components, an ORNL design curve for HBU fuel rods was developed to account for this degradation, which is likely caused by stress concentrations at pellet discontinuities during bending. However, the potential detrimental effect of a nonzero tensile mean strain in spent nuclear fuel rods due to the rod-internal pressure and bending under gravity was also considered. Initial estimates predict a 7% degradation because of this expected nonzero mean strain. Additional fatigue testing of high burnup fuel rods is recommended to validate this estimate and quantify the potential magnitude of the degradation in performance. The effect of temperature on the fatigue limit of high burnup fuel rods is also discussed and is concluded to be minor. While data at elevated temperatures would be beneficial, there is currently no additional fatigue testing of high burnup fuel rod planned to determine the magnitude of the effect of temperature. Finally, there is a significant gap between the maximum strain amplitude measured in the MMTT (0.0042%) and the fatigue limit of the ORNL design curve for HBU fuel rods (~0.03%), indicating that fatigue damage is not expected during normal transportation conditions. However as noted above, additional fatigue testing is recommended to confirm that that fatigue limit at nonzero-mean strain does not decrease significantly.

This page is intentionally blank

CONTENTS

LIST OF FIGURES

LIST OF TABLES

REVISION HISTORY

Date	Changes
1/13/23	Initial release

ABBREVIATIONS

BWR	boiling water reactor
CIRFT	Cyclic Integrated Reversible-Bending Fatigue Tester
DOE	US Department of Energy
ENSA	Equipos Nucleares S.A., S.M.E.
HBU	high burnup
MMTT	multimodal transportation test
NE	Office of Nuclear Energy
NRC	US Nuclear Regulatory Commission
OD	outer diameter
ORNL	Oak Ridge National Laboratory
PWR	pressurized water reactor
RIP	rod internal pressure
RT	room temperature
Sandia	Sandia National Laboratories
SNF	spent nuclear fuel

ACKNOWLEDGMENTS

The authors thank their US Department of Energy Office of Nuclear Energy sponsor Ned Larson and the Spent Fuel and Waste Science and Technology storage and transportation program leadership for their continued support. The Sister Rod Project would not have been possible without the vision and support of the Electric Power Research Institute, Westinghouse, Framatome, and Dominion Energy.

F2-1. Introduction

The fatigue performance of high-burnup (HBU) light-water reactor (LWR) fuel rods under transportation conditions is a regulatory concern for the disposition of spent nuclear fuel (SNF) [F2-1]. During LWR fuel transportation, the internally pressurized fuel rods are oriented horizontally and experience the vibrations typical of transportation, which cause cyclic bending strains and stresses in the fuel rod. Additionally, the fuel rods may be at an elevated temperature (100–250°C). Thus, an evaluation of fuel rod bending fatigue must consider the following questions.

- What is the expected cyclic history during transportation?
- What is the effect of elevated temperature on fatigue performance?
- What is the effect of the rod internal pressure (RIP) and bending under gravity, which are preloads on the cladding?
- What is the effect of the fuel pellet, which is in contact with, and chemically bonded to, the cladding at HBU?

Using the standard approach to design for fatigue, failures are not expected to occur when the accumulated fatigue damage ratio (D_{fat}) [F2-18] is less than 1.0:

$$D_{fat} = \sum_i^n \frac{N_i}{N_{f(i)}}, \tag{F2-1}$$

where N_i is the expected number of cycles at condition i, $N_{f(i)}$ is the number of cycles that causes failure at condition i, and n is the number of different conditions needed to represent the cyclic history experienced by the component. This method of design for fatigue is only applied when the expected cyclic history contains conditions above the fatigue or endurance limit. When the expected cyclic history conditions are less than the fatigue limit, which is typical for transportation, fatigue damage and thus failure is shown to not occur when[1]:

$$\varepsilon_{a,expected} < \varepsilon_{a,limit}, \tag{F2-2}$$

where $\varepsilon_{a,expected}$ or $\sigma_{a,expected}$ is a conservative representation of the expected cyclic history, and $\varepsilon_{a,limit}$ or $\sigma_{a,limit}$ is the fatigue or endurance limit defined as the strain or stress amplitude in which fatigue damage does not occur. This is often defined as the stress/strain amplitude that causes fatigue failure at 1×10^7 cycles.

The fatigue response of a material or component represented by $N_{f(i)}$ cycles and the fatigue limit, $\varepsilon_{a,limit}$, is determined through cyclic fatigue testing of components. Because most of the cycles to failure are needed for initiation rather than propagation, features inherent in the material or component (e.g., surface roughness, nonhomogeneous cross sections, heat-affected zones, welds, residual stress, stress concentrations) are important to consider when testing for fatigue. Additionally, to provide the necessary confidence in predicting that fatigue failures do not occur, conservatism is added to create a design fatigue curve (N_f^{design}) where the design fatigue limit ($\varepsilon_{a,limit}^{design}$) is the strain amplitude at $N_f^{design} = 1x10^7$. Depending on the certainty in the expected cyclic history and consequence to failure, conservatism may also be added by making a design cyclic history more severe than the expected cyclic history. One source of conservatism when the actual number of cycles at $\varepsilon_{a,expected}$ is small is that it is assumed to occur over

[1] The calculation of fatigue damage is not meaningful when the expected cyclic history is below the fatigue limit because it requires extrapolation of the fatigue curve well beyond the range of the data.

1×10^7 cycles, consistent with the fatigue limit. As an example, the expected number of cycles near an expected strain amplitude (i.e., above the noise) in the MMTT test were ~4000 cycles [F2-31].

This report provides a fatigue evaluation of SNF rods based on testing irradiated and unirradiated cladding alloys [F2-2]–[F2-12] and irradiated fuel rods [F2-14]–[F2-19] to create a design fatigue curve so that a design fatigue limit can be compared with an expected cyclic history based on shipping tests [F2-20]–[F2-21].

The evaluation begins with a review of the fatigue data for Zr alloys and the O'Donnell-Langer correlations. These data are compared with fatigue testing on HBU fuel rods[2], and the comparison shows a degradation in fatigue performance of fueled rod segments when compared with estimates based on Zr alloy fatigue test data. A modified version of the O'Donnell-Langer design curve referred to herein as the ORNL Fuel Rod design curve is then developed based on the irradiated fuel rod test data, but there are two potential non-conservatisms in the fuel rod data that require further evaluation: (1) the fatigue testing was performed under zero-mean strain conditions, whereas the fuel rod will be under nonzero mean tensile strain conditions, which tends to degrade fatigue performance (see Section 4), and (2) the testing is performed at RT, whereas the fuel rods are at elevated temperature during transportation. These potential non-conservatisms are discussed, and additional testing is identified where necessary to quantify the effect.

[2] O'Donnell-Langer data was collected on flat samples in reversible bending and rod samples in reversible axial fatigue tests where the strain amplitude was controlled [F2-2]. The HBU fuel rods were tested in reversible bending using the ORNL CIRFT system under load control where strain is calculated from the measured curvature in the test [F2-13].

F2-2. Background

F2-2.1 Stress Amplitude vs. Strain Amplitude

Fatigue testing is performed by applying an alternating stress or strain amplitude and counting the number of cycles to failure.

The fatigue response of a material may be different under stress-controlled fatigue than under strain-controlled fatigue because of the nonlinear behavior of ductile materials. When work hardening occurs during a stress-controlled fatigue test, the maximum strain decreases for a given stress amplitude because work hardening increases the yield strength. In contrast, if the test is performed under strain control, then the stress will increase for the applied strain amplitude. Because of the nonlinear behavior in ductile materials, there may be differences in the plastic energy associated with the hysteresis curve for the two different loading conditions in the low-cycle fatigue regime. However, in the high-cycle regime where the stress and strain are well within the elastic regime, the difference in the two loading conditions is minimal. This justifies measuring high-cycle fatigue data under strain-controlled conditions but reporting the data in terms of stress, which is the approach that O'Donnell-Langer used when developing the fatigue design curves for Zircaloy [F2-2].

Another factor of an SNF rod is that under bending, the stress distribution through the composite rod is nonlinear, which contrasts with the linear stress distribution in a homogeneous material. Thus, there is the potential for confusion regarding how stress is calculated. From a fatigue performance perspective, it is more logical to account for the nonlinear stress distribution, but it is easier to assume that the rod is a homogeneous material in a finite element evaluations of transportation conditions. Unlike stress, the strain distribution remains linear in the composite spent fuel rod under bending. Thus, the measured and predicted strains on the cladding surface will be consistent, regardless of how the spent fuel rod is modeled.

Finally, it is better to present the fatigue data in terms of strain amplitude because the strain-amplitude fatigue limit can be compared directly to measurements of strain amplitude (on the cladding surface) in surrogate fuel rods that have experienced transportation conditions [F2-20].

F2-2.2 Zirconium Alloy Fatigue

The starting point for creating a design fatigue curve for SNF is to understand the fatigue behavior of Zr alloy cladding materials [F2-2]–[F2-10]. O'Donnell and Langer [F2-2] remains the definitive work for fatigue behavior of Zircaloy when designing Zr components for nuclear power applications. O'Donnell-Langer developed design fatigue curves for both unirradiated and irradiated Zircaloy over a temperature range from room temperature (RT) to 315°C (600°F), although all the high-cycle fatigue data were exclusively at 315°C. The use of the high-temperature data to represent fatigue at RT was considered conservative because the data indicated better fatigue performance at RT [F2-2]. The best estimated fatigue limit of both unirradiated and irradiated Zircaloy-2 was reported in terms of zero-mean stress amplitude as 24,790 psi (171 MPa) and 25,730 psi (177 MPa), respectively. Thus, irradiation exposure ranging from 1.5×10^{21} n/cm^2 to 5.5×10^{21} n/cm^2 did not significantly affect the fatigue performance of Zircaloy-2. Considering these are essentially equivalent, the corresponding fatigue limit in terms of zero-mean strain amplitude is 0.2%[3] (See Table F2-1). This result contrasts with later work by Nakatsuka et al. [F2-3] in which irradiation decreased the fatigue limit from 0.22% for unirradiated Zircaloy-2 to 0.18% for irradiated Zircaloy-2 at a test temperature of 350°C (660°F). Like O'Donnell and Langer, Snowden et al. [F2-4] found that any temperature effect on fatigue of cladding alloys is minor so that fatigue curves based on data between 300 and 350°C (570 and 660°F) are applicable to RT. However, the fatigue limit of unirradiated

[3] This conversion (dividing the stress-based endurance limit by the Young's modulus) is valid because the testing was performed at constant strain amplitudes rather than at constant stress amplitudes, and the stresses are well within the elastic regime.

Zircaloy at RT was reported from 0.25% [F2-4] (calculated from stress amplitude of 235 MPa) to ~0.5% [F2-12], which is significantly different than data at higher temperatures [F2-2], [F2-3], [F2-5], [F2-6]. For example, fatigue testing from Wisner et al. [F2-5] on unirradiated Zircaloy-2 indicated that the fatigue limit at 343°C (650°F) was less than 0.14%. Because the transportation of SNF may occur at elevated temperatures, these observations suggests that the effect of temperature on the fatigue performance of irradiated fuel rods should be considered, as discussed in Section F2-5.

Table F2-1 Reported fatigue limits for Zircaloy-2 and Zircaloy-4 under various test conditions

Material	Test Conditions	Reported Fatigue Limit	Reference
Zircaloy-2	Zero-Mean Strain, Irradiated and Unirradiated, 315°C,	0.2%	[F2-2]
Zircaloy-2	Zero-Mean Strain, Irradiated, 350°C	0.18%	[F2-3]
Zircaloy-2	Zero-Mean Strain, Uniradiated, 350°C	0.22%	[F2-3]
Zircaloy-2	Zero-Mean Strain, Unirradiated, R.T.	0.25%	[F2-4]
Zircaloy-4	Zero-Mean Strain, Unirradiated, R.T.	~0.5%	[F2-12]
Zircaloy-2	Zero-Mean Strain, Unirradiated, 343°C	<0.14%[a]	[F2-5]

[a] Wisner et al. measured a fatigue life of 283091 cycles at a strain amplitude of 0.14%.

The standard geometry test samples used in previous tests are flat plates tested in bending or rods tested in the axial direction [F2-2]. In each case, the entire surface area of the sample experiences the maximum strain at the peaks of the fatigue cycles. Pure bending of a rod or tube is different in the sense that the maximum strain in bending occurs only on a line over the surface rather than over the entire surface area. Thus, the volume of material that experiences the maximum strain during testing is significantly smaller than a standard geometry sample. To explore this potential sample geometry effect, Zircaloy-4 cladding tube samples were fatigue-tested in bending using the Cyclic Integrated Reversible-Bending Fatigue Tester (CIRFT) (Section F2-2.4) and compared with the fatigue data from standard sample geometries [F2-13]. These data are replotted in Figure F2-1, where the mean strain is the average of the maximum and minimum strain during testing, which is zero in this case. The Zircaloy-4 cladding-only data are consistent with other Zircaloy-4 data that used a standard sample geometry but are generally higher than the Zircaloy-2 data, as represented by the best-estimate correlation from O'Donnell-Langer for irradiated Zircaloy [F2-2]. This could be because there are differences in composition or because the O'Donnell-Langer correlation is based on fatigue testing at 315°C (600°F). The conclusion from testing the cladding-only sample geometry is that fatigue performance is not affected by sample geometry.

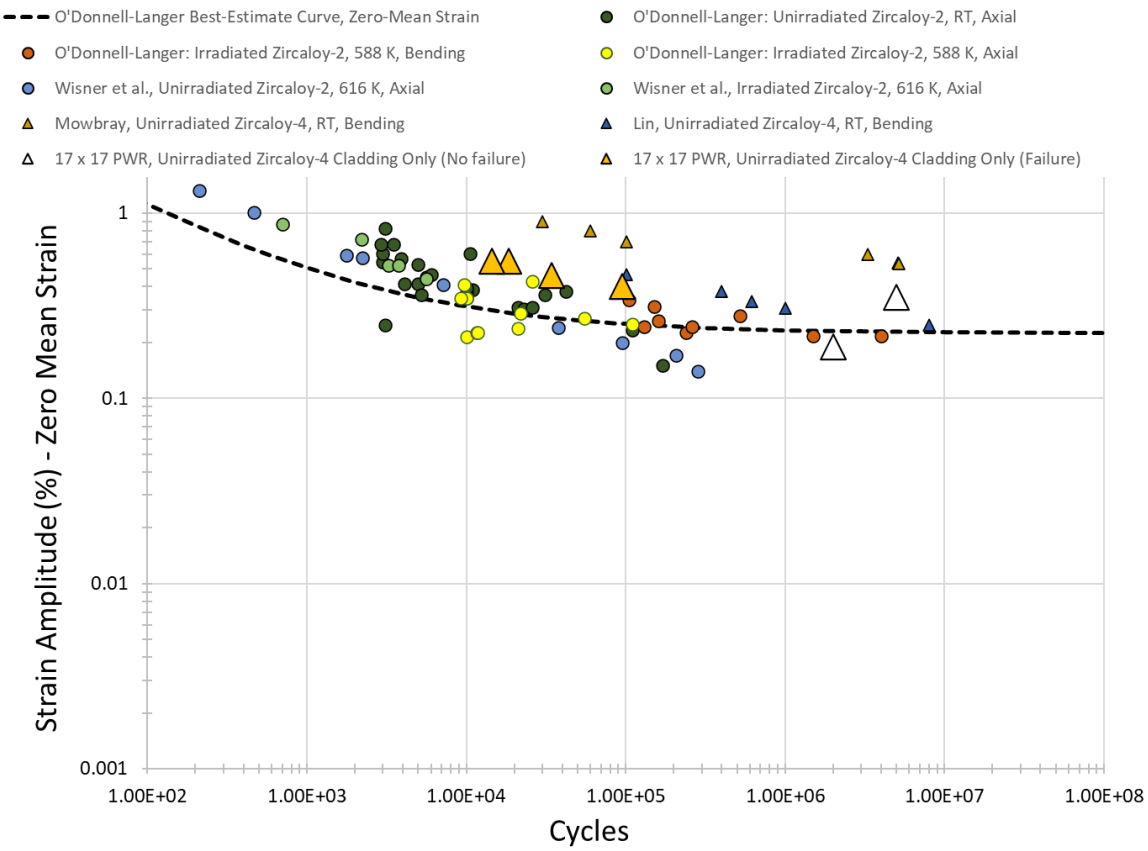

Figure F2-1. Fatigue response of unirradiated and irradiated Zircaloy for various sample geometries and temperatures.

F2-2.3 The O'Donnell-Langer Fatigue Curve

The original O'Donnell-Langer fatigue curve [F2-2] was in the form of stress vs. fatigue cycles, as shown in Eq. (F2-3):

$$S = \frac{E}{F_c\sqrt{N}} \ln \frac{100}{100-RA} + S_e, \tag{F2-3}$$

where S is the stress amplitude that causes fatigue failure at N cycles; S is calculated from the applied range of strain as $\frac{1}{2}\varepsilon_{range}E$; E is the elastic modulus; F_c is a constant that is equal to 4; RA is the reduction in area of a tensile test but is effectively used as a fit parameter; and S_e is the endurance limit or fatigue limit below which fatigue failure is not expected for a practical number of fatigue cycles.

This model can be redefined in terms of the strain amplitude (ε_a) by dividing Eq. (F2-3) by the elastic modulus to give

$$\varepsilon_a = \frac{1}{F_c\sqrt{N}} ln \frac{100}{100-RA} + \varepsilon_e, \tag{F2-4}$$

where ε_e is the fatigue limit in terms of strain amplitude. The strain-based parameters of the O'Donnell-Langer model for irradiated Zircaloy shown in Figure F2-1 are provided in Table F2-2.

Table F2-2. O'Donnell-Langer Best-estimate curve for irradiated Zircaloy (zero-mean strain).

	Parameters for Eq. (F2-4)*
RA	30
ε_e	0.0022
F_c	4

* These values are calculated from the stress-based O'Donnell-Langer model for irradiated Zircaloy. Because O'Donnell-Langer did not report RA for irradiated Zircaloy, the value of 30 was determined by matching the model predictions to that plotted in Figure 2 of O'Donnell and Langer [F2-2].

F2-2.4 Fatigue of High-Burnup Fuel Rods

The US Nuclear Regulatory Commission (NRC) sponsored the development of the CIRFT system to measure the fatigue performance of various fuel rod designs from both pressurized water reactors (PWRs) and boiling water reactors (BWRs) [F2-14]–[F2-16], and Oak Ridge National Laboratory (ORNL) developed the system. The system can perform reversible cyclic pure-bending testing at either a zero or nonzero mean strain, although in the past, it has only been applied to zero-mean strain conditions [F2-14]–[F2-16]. Three different spent fuel rod types were tested under both NRC and US Department of Energy sponsorship: (1) 15 × 15 PWR fuel rods with Zircaloy-4 cladding, (2) 17 × 17 PWR fuel rods with M5 cladding, and (3) 9 × 9 BWR fuel rods with Zircaloy-2 cladding [F2-16]. Additionally, CIRFT testing of 17 × 17 PWR fuel rods with Zircaloy-4, M5, and ZIRLO cladding was completed as part of the Sister Rod Project [F2-17]. The exposures in this database range from 45 to 67 GWd/MTU rod-average exposure. These data are replotted in Figure F2-2 and show a significant degradation in the high-cycle fatigue performance of the HBU fuel rods compared with the performance of Zr alloys.

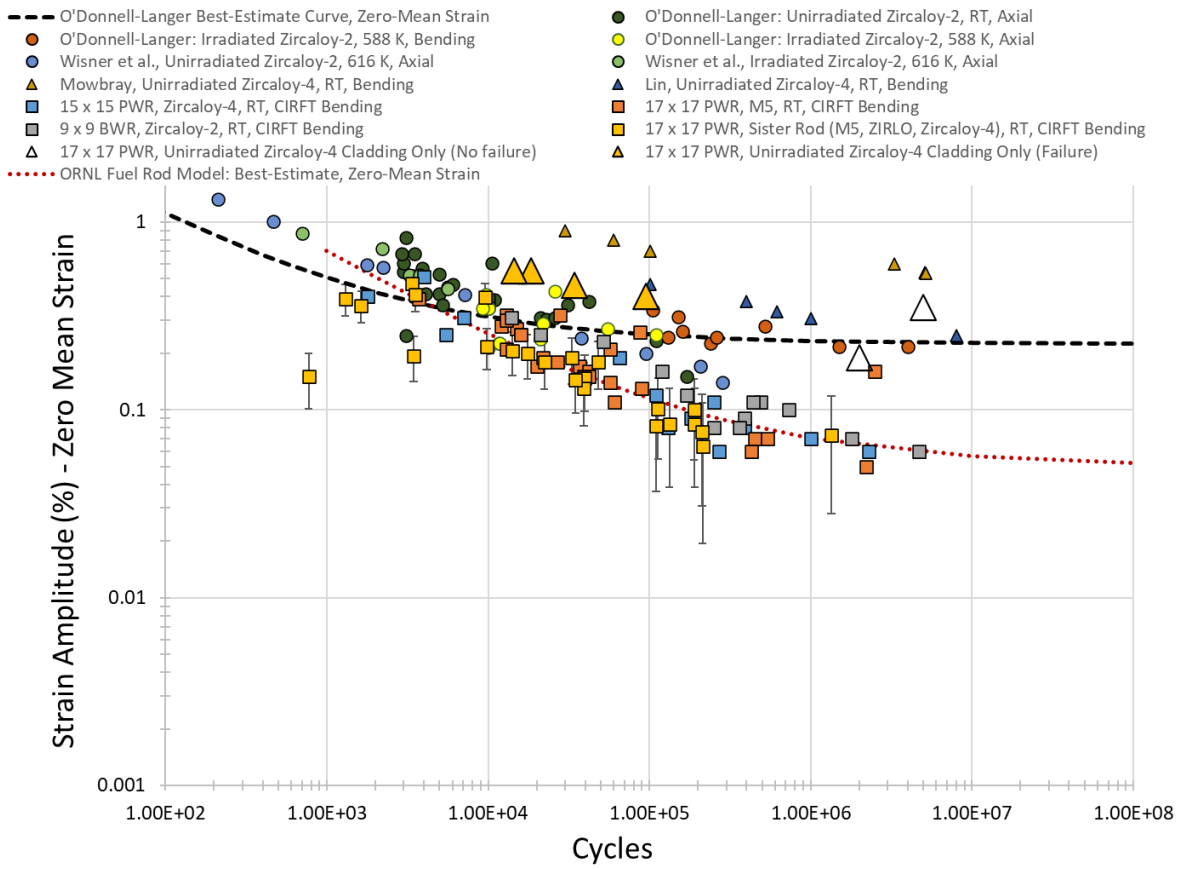

Figure F2-2. Fatigue of HBU fuel rods compared with Zr alloy and cladding-only test data. Note the strain amplitude of the HBU fuel rod data is calculated from the measured curvature in the CIRFT tests [F2-13]

The best estimate correlation through the 17 × 17 PWR fuel rod data is the ORNL Fuel Rod correlation. Table F2-3 provides the parameters of Eq. (F2-4).

Table F2-3. ORNL Fuel Rod best-estimate curve for 17 × 17 PWR fuel rods (zero-mean strain).

	Parameters for Eq. (F2-4)
RA	56
ε_e	0.0005
F_c	4

One outcome of fatigue-testing fuel rods was the recognition that discontinuities in the pellet (e.g., pellet cracks, pellet-to-pellet interfaces) (Figure F2-3) cause stress concentration in HBU (45–70 GWd/MTU rod-average exposure) fuel rods under bending [F2-16]–[F2-19]. Because fatigue failures initiate at the high-stress/high-strain locations, the increase in local stress/strain in the cladding near the discontinuities in the pellet causes the observed decrease in fuel rod fatigue performance compared with the performance of the cladding alone. The magnitude of the stress/strain concentration can be estimated as the ratio of the fatigue limit for cladding alloys to that of the HBU fuel rods (0.2%/0.06% = 3.3).

Best estimate correlations are typically not used for system design or conservative decision-making. Design curves that provide a factor of safety are typically used and are developed in Section 3.

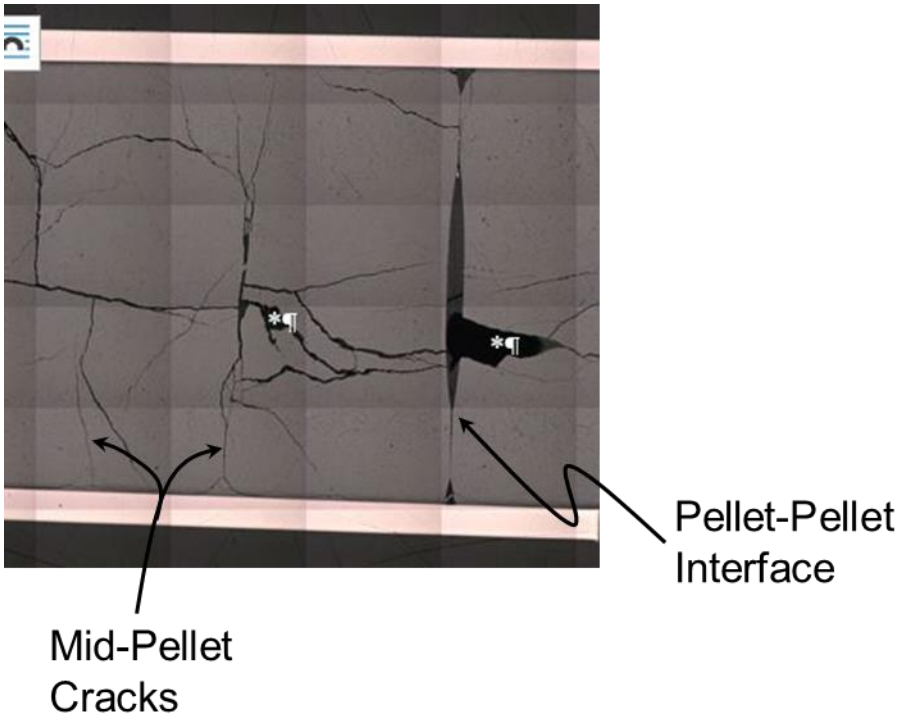

Figure F2-3. Axial cross section of a fuel rod highlighting the discontinuities in the pellet stack.

F2-3. Fatigue Design Curves

For design purposes, O'Donnell-Langer used the lowest of either decreasing the stress/strain amplitude by a factor of two or decreasing the number of cycles by a factor of 20. For high cycle fatigue performance considered herein, the more conservative change is decreasing the stress/strain amplitude by a factor of two, and only this version was considered herein. O'Donnell-Langer [F2-2] did not indicate that these design factors were based on a statistical data evaluation. Rather, they appear to be based on engineering judgement. However, the approach has been universally accepted by industry [F2-32] and thus is a reasonable approach to apply to the ORNL Fuel Rod correlation. The design curve parameters for both Zr alloys and HBU fuel rods are provided Table F2-4, and Figure F2-2 is replotted in Figure F2-4 with both correlations to show that the design curves bounds the data, except the ORNL Fuel Rod design curve does not bound the reported uncertainty in the sister rod data [F2-17]. This exception is discussed in Section F2-6, but the expectation is that fatigue damage does not occur at strain amplitudes below the fatigue limit.

Table F2-4. Correlation parameters for the Zero-Mean Strain O'Donnell-Langer design curve for Zr alloys and the Zero-Mean Strain ORNL Fuel Rod design curve for 17 × 17 PWR fuel rods (zero-mean strain).

	O'Donnell-Langer design curve parameters for Eq. (F2-4)	ORNL Fuel Rod design curve parameters for Eq. (F2-4)
RA	30	56
ε_e	0.0011	0.00025
F_c	8	8

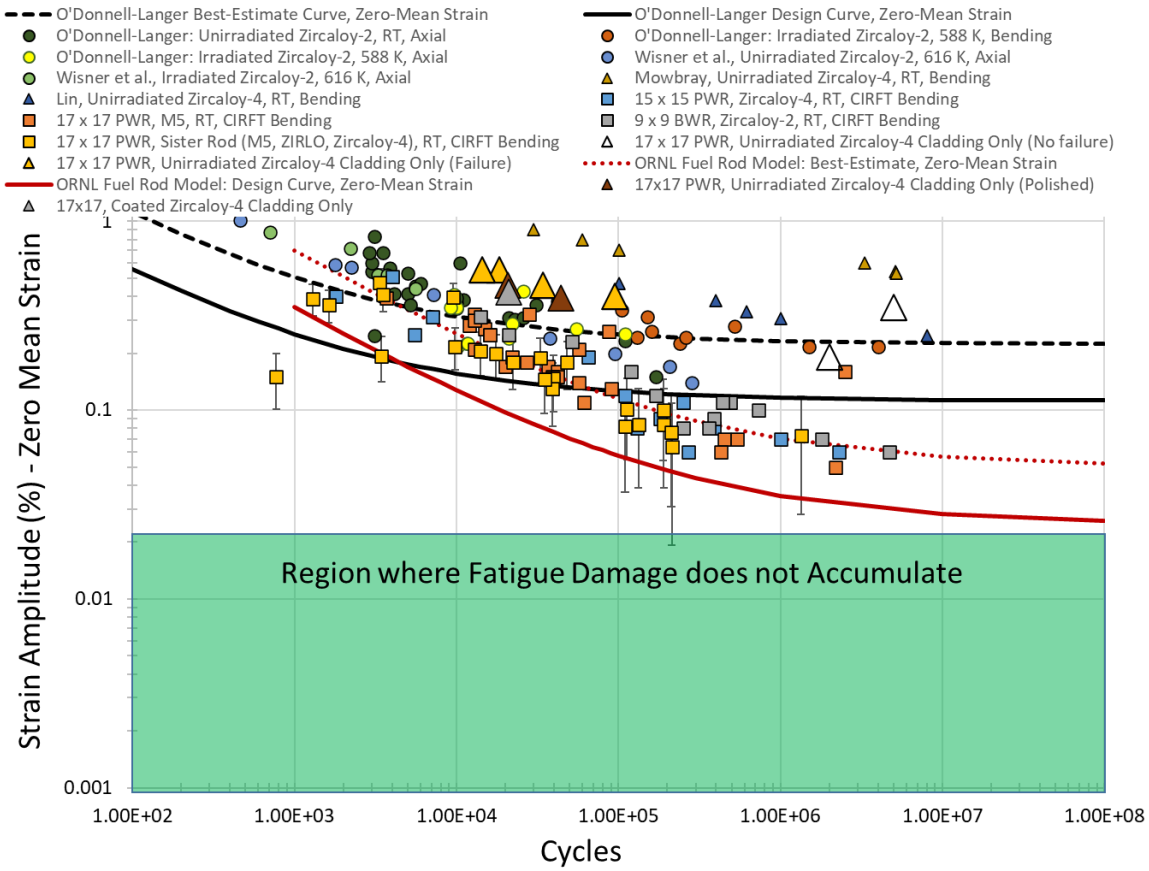

Figure F2-4. Fatigue of HBU fuel rods compared with Zr alloy and cladding-only test data, including fatigue design curves.

F2-3.1 Limitation of Applicability

Consistent with NUREG-2224 [F2-18], the applicability of the ORNL Fuel Rod design curve is limited to loading of HBU fuel rods (45-67 GWd/MTU, rod average exposure) in bending where the cyclic strain is in the axial direction. This design curve is not applicable to evaluating the fatigue performance when the cyclic strain is in the hoop direction.

F2-4. Effect Of Nonzero-Mean Strain

Traditionally, fatigue testing is performed at zero-mean strain, which means the testing is performed in a reversible manner so that the average strain ($\frac{\varepsilon_{max}+\varepsilon_{min}}{2}$) is zero. However, fatigue in real components is rarely under a zero-mean strain condition. In most cases, the components are under load when experiencing fatigue cycles, and when the load is tensile this causes a decrease in the fatigue performance. The best approach is to directly test the effect of a prototypical nonzero-mean tensile strain on the fatigue performance and then multiply the zero-mean strain design curve by the observed degradation factor. These observed degradation factors can then be fit to a correlation, such as the Goodman factor ($1-\frac{\sigma_{mean}}{\sigma_{UTS}}$), which can then be applied more generically in design. O'Donnell and Langer [F2-2] considered the effect of mean tensile strain using a degradation factor that was validated by fatigue testing performed under conditions in which the mean tensile strain was 1% [F2-12]. The O'Donnell-Langer degradation factor for mean strain is:

$$\frac{\sigma_{UTS}-S_b}{\sigma_{UTS}-S}, \tag{F2-5}$$

where σ_{UTS} is the ultimate strength, S_b is the cyclic yield strength, and S is the stress amplitude defined in Eq. (F2-3). For irradiated Zircaloy, O'Donnell and Langer [F2-2] reported that ultimate strength was between 60 and 70 ksi (410–480 MPa), and the cycle yield strength was measured as 34 ksi (~230 MPa).

Because the testing performed on spent fuel rods was under zero-mean strain conditions, the design curve in Figure F2-4 may be nonconservative given that internal gas pressure and bending under gravity cause cladding strain that results in a nonzero-mean tensile strain. The following section evaluates those strains to determine whether they are significant.

F2-4.1 Method for Calculating the Effects of Bending under Gravity

To assess the magnitude of static bending stress and strain when the rod is transported in a horizontal orientation, simple beam correlations are used, assuming a uniform load as a function of the mass of the rod times gravity. For a PWR rod, the deflection and slope at the spacer grid locations is assumed to be zero (Figure F2-5), except at the ends of the rods where there is no neighboring grid (Figure F2-6).

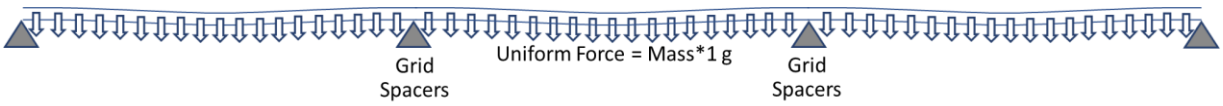

Figure F2-5. Schematic of a fuel rod under gravity between grid spacers.

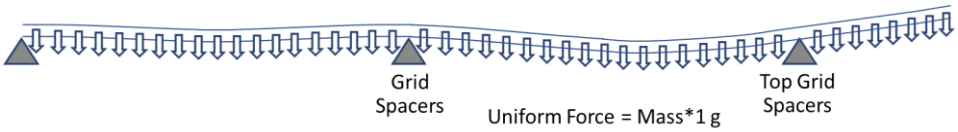

Figure F2-6. Schematic of a fuel rod under gravity near the top of the assembly where the top or bottom end plug is not constrained.

In BWRs, the top and bottom ends of the rods are constrained so that the PWR condition is conservative. Thus, by assuming that both ends are simply constrained, the maximum deflection and strain will be more conservative than the most limiting section at the top or bottom of the PWR assembly.

A schematic of a simply supported beam with a uniform load is shown in Figure F2-7, and the deflection is calculated by Eq. (F2-6) [F2-22]:

$$\Delta_x = \frac{wx}{24EI}(l^3 - 2lx^2 + x^3). \quad \text{(F2-6)}$$

where Δ_x is the displacement (mm) from horizontal as a function of x, x is the distance from the left most simple support (mm), l is the length of the span between the spacer grids (mm), w is the uniform load (N/mm), and EI is the flexural rigidity of the fuel rod (N-mm^2).

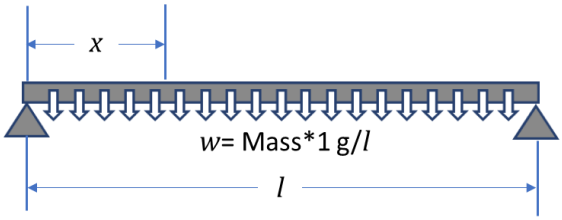

Figure F2-7. Schematic of a simple beam with a uniform load.

The maximum moment at the midpoint of the span is [F2-22]:

$$M_{max} = \frac{wl^2}{8}. \quad \text{(F2-7)}$$

The dimensions used in this evaluation for the various fuel rod types are provided in Table F2-5. The burnup of the fuel rods is assumed to be high enough to close the gap between the pellet and cladding. Thus, the cladding thickness is the rod outer diameter [OD] minus the pellet OD, then divided by two. This information is used to calculate the mass between the spacer grids.

Table F2-5. Dimensions assumed for the various fuel rod types.

	17 × 17 PWR	15 × 15 PWR	9 × 9 BWR
Fuel rod (or Cladding) OD (mm)	9.45 [F2-23]	10.7 [F2-24]	11.4 [F2-27]
Pellet OD (mm)	8.3 [F2-23]	9.25 [F2-24]	10.1**
Flexural rigidity at RT (N-m^2)	26 [F2-26]	41*	50***

* Calculated as average of flexural rigidity data reported in Table 2 of Wang et al. [F2-27].
** Estimated as fuel rod OD minus 2 × 0.66 mm (cladding thickness reported in NUREG-1754 [F2-25]).
*** Calculated as average of LMK data reported in Table 6b of Wang et al. [F2-24]. (LMK01 was excluded because it was static tested before dynamic testing.)

For calculating the mass, the pellet density was 10.8 g/cm^3 (98.5% of theoretical density,10.97g/cm^3), and the cladding density was 6.5 g/cm^3.

The radius of curvature at the midpoint is calculated from the maximum moment and flexural rigidity as

$$\rho = \frac{EI}{M_{max}}, \quad \text{(F2-8)}$$

The maximum cladding surface strain in the axial direction over the region in pure bending can then be calculated using the standard beam theory relationship:

$$\varepsilon_b = \frac{OD/2}{\rho}. \quad \text{(F2-9)}$$

F2-4.2 Method for Calculating the Axial Cladding Strain due to Gas Pressure

The purpose of this calculation is only to determine if the mean strain is potentially significant compared to the fatigue performance, which will help determine whether testing of pressurized segments (capturing the nonzero mean strain effects) is valuable. Two methods are defined to calculate a minimum and maximum axial strain, thus defining the potential range. The first method assumes that the gas pressure is only applied at the ends of the fuel rod and the resulting axial strain are uniform over the entire length of the cladding. This method defines the minimum of the range. The second method assumes the pellets are largely bonded to the cladding, which effectively localizes the axial strain at pellet-pellet interfaces. This method defines the maximum of the range.

F2-4.2.1 Method for Calculating Average Axial Cladding Strain

The average axial cladding strain is calculated assuming the fission gas pressure at end-of-life is modelled as an internally pressurized closed tube (see Figure F2-8), which induces biaxial tension with an approximate 2:1 ratio for the hoop-to-axial directions.

The cladding hoop stress can be estimated by:

$$\sigma_h = P\frac{OD_{pellet}}{(OD_{cladding} - OD_{pellet})}, \quad \text{(F2-10)}$$

where P is the internal pressure; OD_{pellet} is the outer diameter of the pellet or inner diameter of the cladding; and $OD_{cladding}$ is the outer diameter of the cladding.

The average axial stress in the fuel rod due to gas pressure is then:

$$\sigma_{z-average} = P\frac{(OD_{pellet}/2)^2}{\left(\frac{OD_{cladding}}{2}\right)^2 - \left(\frac{OD_{pellet}}{2}\right)^2}. \quad \text{(F2-11)}$$

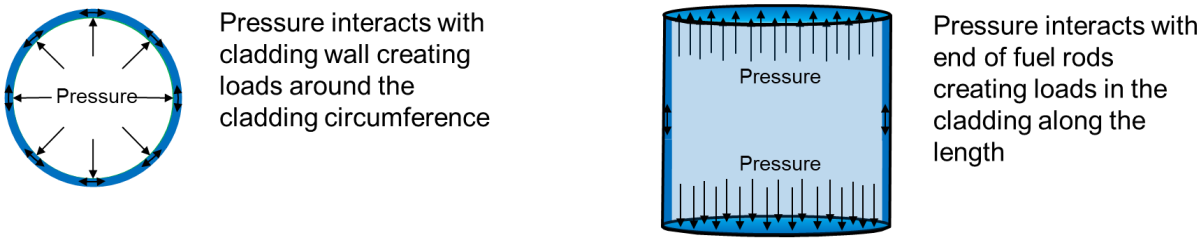

Figure F2-8. Schematic of how the pressure applied load in an internally pressurized tube.

The average axial cladding strain for an internally pressurized tube is then

$$\varepsilon_{z-average} = \frac{\sigma_{z-average}}{E_{clad}} - \nu\frac{\sigma_h}{E_{clad}}, \quad \text{(F2-12)}$$

which accounts for the negative strain from the hoop stress due to the Poisson effect.

F2-4.2.2 Method for Calculating Local Axial Cladding Strain

In a high-burnup fuel rod, the stress state in the cladding of an SNF rod due to the fission gas pressure at end-of-life is complicated by the observation of chemical bonding between the pellet and cladding and the crack structure within the pellet where the fission gas resides. While there are often circumferential cracks in the pellet near the pellet-cladding interface, which might be considered a gap, there are also many areas where no such gap is obvious (see Figure F2-9). Under these circumstances, the internal pressure will not apply uniformly to the cladding like an internally pressurized tube. Rather, the fission gas will apply force to the cladding through pellet pieces. Another consideration in dry storage is that there will likely be some temperature distribution in the pellet, which could create pressure distributions. Given the low thermal conductivity of the fuel pellet, it is reasonable to conclude the maximum temperature would be at the center of the pellet, meaning the fission gas pressure of the internal cracks would dominate over the pressure in the circumferential cracks near the cladding, which pushes the pellet pieces against the cladding. The forces from internal gas pressure are then applied to the cladding through the solid pellet.

Another important implication of the forces being transferred through a solid-solid interface is that there will be frictional forces at the interface, as opposed to the case when gas is in direct contact with the tube and the frictional forces at the interface are zero. In high-burnup fuel rod, the axial stress in the cladding will be non-uniform. A schematic of a pellet stack in a high burnup fuel rod is provided in Figure F2-10. Assuming the pellets are bonded to the cladding, the axial cladding stress in the region in contact with the pellet will be a combination of the compressive stress due to the pressure compressing the pellet in the axial direction and the tensile stress caused by the pellet constraining the Poisson contraction in the axial direction due to the cladding hoop stress (i.e., the plane strain assumption, see Figure F2-10b).

In contrast, the local axial tensile stresses at the pellet ends can be estimated based on the schematic in Figure F2-10c. In this region the pressure acts on the pellet ends, which induces an axial tensile stress (and strain) that is equivalent to the average axial stress and strain prediction. However, it is further assumed that there is sufficient contact between the pellet ends to constrain the Poisson contraction from the hoop stress, which means that the second term in Eq. 12 is now zero. Thus, the local axial cladding strain in the cladding near a pellet-pellet interface is then defined as

$$\varepsilon_{z-local} = \frac{\sigma_{z-average}}{E_{clad}}, \tag{F2-13}$$

F2-4.3 Total Estimated Additional Strain Due to Static Bending and Rod Internal Pressure

The total axial cladding strain on the cladding surface is then Eq. (F2-9) plus Eq. (F2-12) or Eq. (F2-13):

$$\varepsilon_T = \varepsilon_b + \varepsilon_z. \tag{F2-14}$$

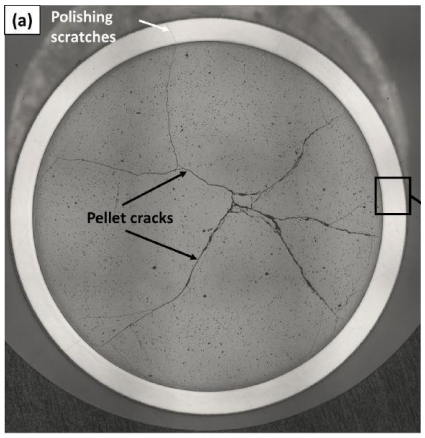

a) Pellet cracks in an M5 fuel rod 30AE14 (elevation = ~1685 mm, Figure B-9a from [F2-23])

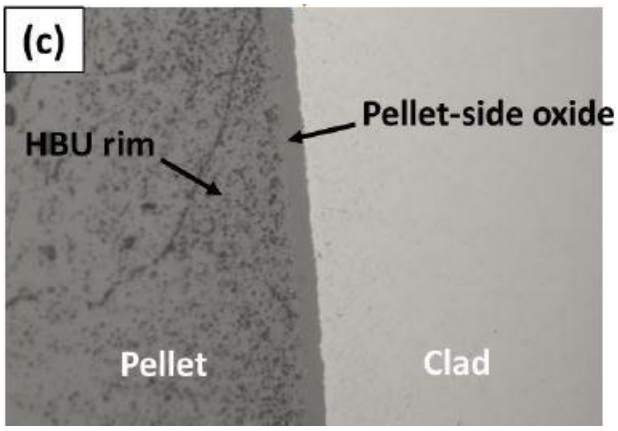

b) Pellet-cladding interface in a region where there is not clear circumferential cracking that could be considered a gap (Figure B-9c from [F2-23])

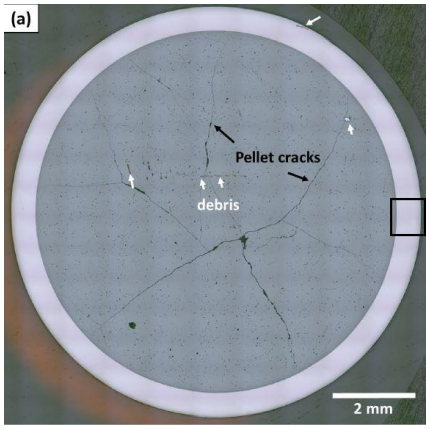

c) Pellet cracks in an M5 fuel rod 30AE14 (elevation = ~2210 mm, Figure B-10a from [F2-23])

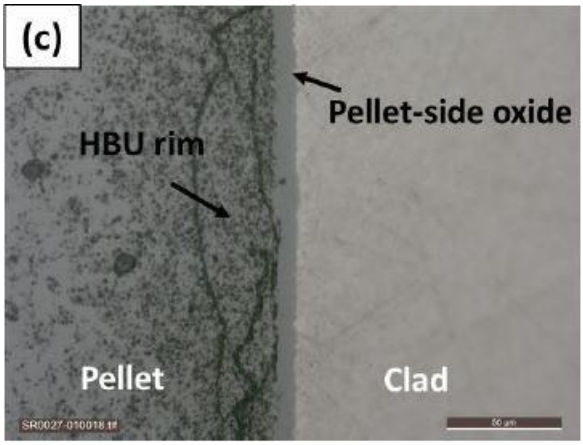

d) Pellet-cladding interface in a region where there is clear circumferential cracking that could be considered a gap (Figure B-10c from [F2-23])

Figure F2-9. Observations of microstructure at pellet-cladding interface

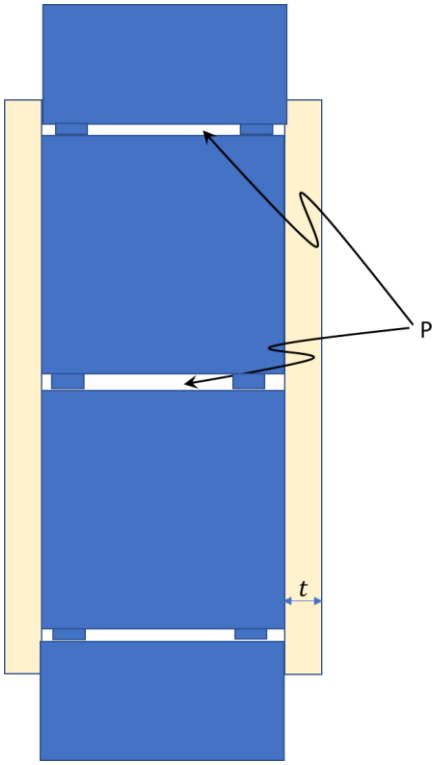

a) An idealized representation of a pellet stack in a high burnup fuel rod where the pellet and cladding are bonded and the pellet ends are in contact but not bonded

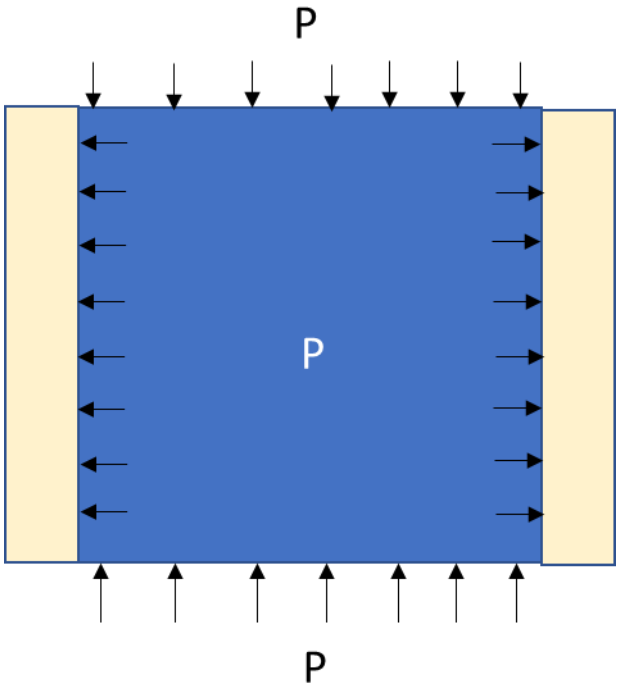

b) schematic of how pressure within the pellet interacts with bonded cladding.

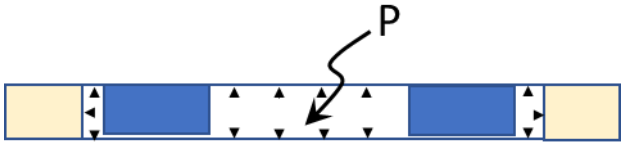

c) schematic of how the pressure at the pellet ends interacts with the cladding. The pellet features shown will resist the Poisson contraction in the axial direction due to the local hoop stress.

Figure F2-10. Schematic of how pressure interacts with the pellet ends when the pellets are bonded to the cladding,

F2-4.4 Cladding Strain Results and Discussion

The calculated maximum strains for horizontally oriented fuel rods under gravity are provided in Table F2-6 for different spans between the grid spacers. Although the 17 × 17 PWR fuel rod is predicted to have the highest strains under gravity, there is very little difference between the designs. This indicates that as mass increases (causing more strain) and flexural rigidity increases (causing less strain) with rod diameter, the effects nearly cancel each other out. Currently, it is assumed that the calculated strains from bending at RT

apply to higher temperatures. However, flexural rigidity is expected to decrease at elevated temperature because of the decrease in Young's modulus of both the cladding and the pellet, which would tend to increase the bending strains. This effect likely can be accounted for by added conservatism when defining the expected cyclic strain history. The typical span in PWR and BWR fuel is between 500 and 550 mm.

Table F2-6. Calculated maximum surface strain from bending in the fuel rod under gravity at RT.

Span length (mm)	Maximum bending strain (%)		
	17 × 17 PWR	15 × 15 PWR	9 × 9 BWR
400	0.0025	0.0022	0.0023
450	0.0031	0.0028	0.0029
500	0.0038	0.0035	0.0035
550	0.0046	0.0042	0.0043
600	0.0055	0.0050	0.0051
650	0.0065	0.0059	0.0060
700	0.0075	0.0068	0.0069
750	0.0086	0.0079	0.0080

When considering the effect of internal pressure on axial strain, the 17 × 17 PWR fuel rod exhibited the highest axial strain at a given pressure. Thus, the 17 × 17 PWR fuel rod represents the conservative condition when compared with the 15 × 15 PWR and 9 × 9 BWR fuel rods. The effect of the internal pressure on the local (max) and average (min) axial strain in a 17 × 17 PWR fuel rod is provided in Table F2-7. There is almost an order of magnitude difference in the min and max predicted strains.

Based on the data in Figure C-10 of Morris and Montgomery [F2-29], an approximate RIP at RT can be estimated for different rod-average burnups. For 50 GWd/MTU, the estimated RIP is 4 MPa; for 70 GWd/MTU, the estimated RIP is 6 MPa; for 80 GWd/MTU, the estimated RIP is 7 MPa. Given this input, the predicted maximum axial strain caused by RIP at the potential transportation temperatures for each burnup level is provided in Table F2-8. The effect of adding the bending strains to the strains due to RIP are provided in Table F2-9. Thus, the total maximum axial strain is estimated to vary from ~0.02 to ~0.06%, depending on burnup and temperature during transportation. The corresponding minimum range in axial strain is ~0.007 to ~0.012%

Table F2-7. Calculated minimum and maximum axial strain in a 17 × 17 PWR fuel rod from internal gas pressure at RT for 150 and 250°C axial strain.

Pressure	Hoop stress	Axial stress	RT Average axial strain (min)	RT Local axial strain (max)	150°C Average axial strain (min)	150°C Local axial strain (max)	250°C Average axial strain (min)	250°C Local axial strain (max)
(MPa)	(MPa)	(MPa)	(%)	(%)	(%)	(%)	(%)	(%)
2	14.4	6.7	0.001	0.007	0.001	0.008	0.001	0.008
3	21.7	10.1	0.002	0.011	0.002	0.012	0.002	0.013
4	28.9	13.5	0.002	0.015	0.002	0.016	0.002	0.017
5	36.1	16.9	0.003	0.018	0.003	0.020	0.003	0.021

Table F2-7. Calculated minimum and maximum axial strain in a 17 × 17 PWR fuel rod from internal gas pressure at RT for 150 and 250°C axial strain, continued.

Pressure	Hoop stress	Axial stress	RT Average axial strain (min)	RT Local axial strain (max)	150°C Average axial strain (min)	150°C Local axial strain (max)	250°C Average axial strain (min)	250°C Local axial strain (max)
6	43.3	20.2	0.003	0.022	0.003	0.024	0.004	0.025
7	50.5	23.6	0.004	0.026	0.004	0.028	0.004	0.029
8	57.7	27.0	0.004	0.029	0.005	0.032	0.005	0.034
9	65.0	30.4	0.005	0.033	0.005	0.035	0.005	0.038
10	72.2	33.7	0.005	0.036	0.006	0.039	0.006	0.042
11	79.4	37.1	0.006	0.040	0.006	0.043	0.007	0.046
12	86.6	40.5	0.006	0.044	0.007	0.047	0.007	0.051
13	93.8	43.9	0.007	0.047	0.007	0.051	0.008	0.055

Table F2-8. Calculated maximum axial strain due to RIP in a 17 × 17 PWR fuel rod for three burnup conditions where the pressures at 150 and 250°C are based on the pressure at RT, assuming no change in volume of number of moles of gas.

Temp. (°C)	Temp. (K)	Beginning of Life pressure (MPa)	Axial strain (%)	~50 GWd/MTU		~70 GWd/MTU		~80 GWd/MTU	
				Pressure (MPa)	Axial strain (%)	Pressure (MPa)	Axial strain (%)	Pressure (MPa)	Axial strain (%)
25	298	2.0	0.007	4.0	0.015	6.0	0.022	7.0	0.029
150	423	2.8	0.011	5.7	0.022	8.5	0.034	9.9	0.039
250	523	3.5	0.015	7.0	0.029	10.5	0.044	12.3	0.052

Table F2-9. Calculated maximum axial surface strain due to both bending and RIP in a 17 × 17 PWR fuel rod for three burnup conditions where the pressures at 150°C and 250°C are based on the pressure at RT, assuming no change in volume of number of moles of gas.

Temp. (°C)	Temp. (K)	Beginning of Life pressure (Mpa)	Total strain (%)	~50 GWd/MTU		~70 GWd/MTU		~80 GWd/MTU	
				Pressure (Mpa)	Total strain (%)	Pressure (Mpa)	Total Strain (%)	Pressure Mpa	Total Strain (%)
25	298	2.0	0.012	4.0	0.019	6.0	0.026	7.0	0.034
150	423	2.8	0.016	5.7	0.027	8.5	0.038	9.9	0.044
250	523	3.5	0.019	7.0	0.034	10.5	0.049	12.3	0.056

F2-4.4.1 Estimated Effect of Mean Strain on Fatigue Performance

The potential effect of a nonzero mean strain on the fatigue limit can be estimated by various degradation models [F2-2],[F2-33]. The Soderberg relation is one model that is amenable to a strain-based

representation and is considered more conservative than other models [F2-33]. The strain-based version of the Soderberg relation is as follows:

$$\varepsilon_a(\varepsilon_{mean} \neq 0) = \varepsilon_a(\varepsilon_{mean} = 0)\left(1 - \frac{\varepsilon_{mean}}{\varepsilon_{yield}}\right) \quad (15)$$

Based on axial tensile testing of tube material [F2-34], the strain at yield (ε_{yield}) is estimated to be between 0.6% and 0.8%. If the mean strain is assumed to be 0.05% (see Table F2-9) and the strain at yield is 0.7%, the model predicts an ~7% degradation. Like any model, validation testing is needed to determine if the predicted degradation is a reasonable estimate of how fatigue of HPU fuel rods degrades because of a pressure-induced nonzero-mean strain effect.

This page is intentionally blank

F2-5. Effect Of Temperature On Fatigue

O'Donnell and Langer [F2-2] considered the effect of temperature when developing a design curve for Zircaloy-2. O'Donnell and Langer [F2-2] argued that it was applicable to temperatures from 25 to 315°C (77 to 600°F) [F2-2]. The O'Donnell-Langer justification for this conclusion was to base the design limit on elevated test data, recognizing that this was conservative relative to RT data, which typically has better fatigue performance. This trend is observed in Figure F2-11, which indicates better high-cycle fatigue performance at RT compared with elevated temperature.

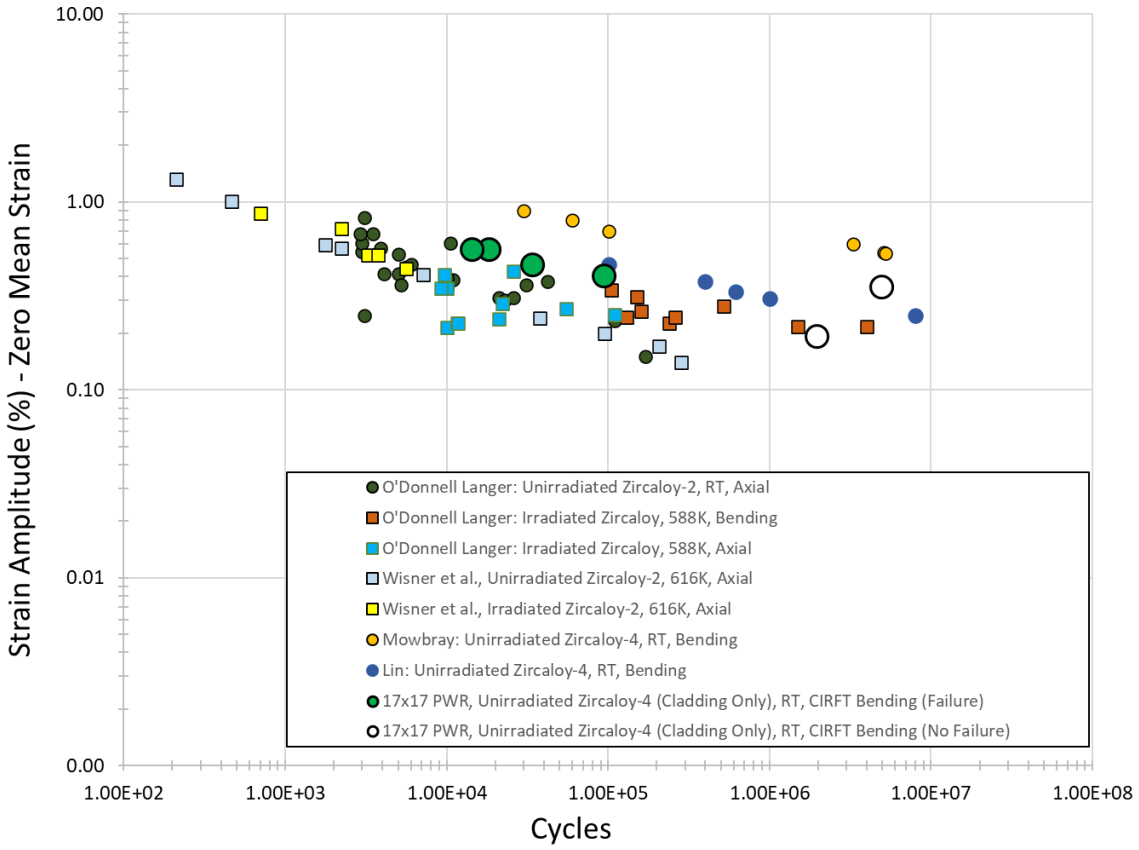

Figure F2-11. Fatigue response of unirradiated and irradiated Zircaloy for various sample geometries and temperatures, highlighting the better fatigue performance at RT (circles) compared with elevated temperatures (squares).

Several additional studies have evaluated the temperature effect on fatigue in Zircaloy, and the general conclusion is that the effect of temperature on fatigue performance from RT to ~400°C is small [F2-4], [F2-8], [F2-10].

The small effect of temperature on the Zircaloy cladding fatigue performance suggests a similar response to temperature should be seen in the fatigue data for the fuel rods. Although fatigue testing at elevated temperature would be beneficial, it is expected that the main effect of temperature on the fuel rod will be increasing the RIP and thus the mean strain. It is expected that once the effect of mean strain is better understood, the design limit based on the RT measurement would be applicable to the higher temperatures during transportation.

This page is intentionally blank

F2-6. Measurement Uncertainty Discussion

The measurement uncertainty of the sister rod CIRFT data was evaluated in Montgomery [F2-30] and is shown in Figure F2-4 with error bars on the datapoints. The analysis found that the relative uncertainty in the data increased as the strain amplitude in testing decreased. For example, the uncertainty at 0.2% strain amplitude was 0.05%, a relative uncertainty of 25%, whereas the uncertainty at 0.06% strain amplitude was approximately 0.04%, a relative uncertainty of 66%. One effect of this large uncertainty at strain amplitudes near the fatigue limit is that the uncertainty is outside the ORNL Fuel Rod design curve (Figure F2-4). To validate these estimated uncertainties, the strain amplitudes calculated based on the CIRFT linear variable differential transformer (LVDT) will be compared with direct measurement of strain amplitude on a cladding-only sample with a strain gage attached to the side that is experiencing the maximum strain. The data from this sample are reported in Wang et al. [F2-26], but the evaluation of the uncertainty has not yet been performed. This is planned as an FY23 activity.

This page is intentionally blank

F2-7. Expected Cyclic History For Transporting Spent Nuclear Fuel

The expected cyclic history for transporting SNF has been considered in shipping tests [F2-20], referred to as the *multimodal transportation test (MMTT)*, and in dynamic modeling of those shipping tests ([F2-21], [F2-31]). The MMTT was an instrumented shipping test of an ENSA ENUN 32P cask that contained three surrogate PWR assemblies in three locations within the basket and 29 dummy assemblies to mimic the expected weight distribution. The three surrogate PWR assemblies had slightly different designs and are designated (1) the Sandia National Laboratories (Sandia) fuel assembly, (2) the ENSA fuel assembly, and (3) the Korean fuel assembly. Each bundle had a few instrumented surrogate fuel rods that comprised of unpressurized unirradiated cladding tubes with either Pb or Mo pellets to represent the mass of UO_2 pellets. Because there is a gap between the pellets and cladding, the flexural rigidity of the surrogate rods should be equivalent to the cladding tube, which is considered conservative compared with HBU fuel. In HBU fuel, the UO_2 is in contact with the cladding, which increases the flexural rigidity and decreases the strains in bending compared with the cladding tube only. The differences in these three assemblies are described in Kalinina et al. [F2-20].

This report focuses on the strain gage and accelerometer data from the center of the surrogate fuel rods, which should represent the location of maximum strain. Based on the nomenclature in Kalinina [F2-20], the accelerometers of interested are A2Z on the Sandia assembly, A7Z on the ENSA assembly, and A11Z on the Korean assembly. The letter "Z" indicates that the accelerometer is measuring accelerations in the vertical direction. The strain gages at the Sandia, ENSA, and Korean fuel assembly locations are SG04-0, SG17, and SG28, respectively. These strain gages were put on top of the surrogate rods after orienting the bundles horizontally and thus do not include the bending strain due to gravity (estimated in Section F2-4).

Considering the strain under gravity, the expected cyclic history can be represented by modifying Eq. (F2-13) to include a time-dependent bending strain:

$$\varepsilon_T(t) = \varepsilon_b(t) + \varepsilon_z, \tag{14}$$

where the bending strain is the bending strain under gravity plus any bending strains associated with accelerations during transportation:

$$\varepsilon_b(t) = \varepsilon_b(1g\ gravity) + \varepsilon_b(transportation\ accelerations(t)). \tag{15}$$

Thus, the MMTT data is a representation of the bending strains associated with accelerations during transportation, and while the MMTT only included standard PWR fuel designs, it has been suggested to be conservative relative to other potential future transportation configuration [F2-21]. Because the observed strain amplitudes in the MMTT are significantly lower than the fatigue limit of the fuel rods, the suggested approach herein is to define a single conservative strain amplitude to bound all expected fuel assembly design and all future transportation configurations. As an example, the maximum observed strain on the fuel assemblies in the MMTT (0.0042%, (Figure 11-10 of [F2-20]) could be used to bound the expected strain amplitudes for the PWR designs tested. This is considered conservative because most cycles are significantly less than this maximum value, and it was observed that only ~4000 cycles occurred above a strain amplitude of 0.001% in the MMTT [F2-31]. To develop a generic strain amplitude that bounds all current and future fuel designs, conservatisms, uncertainties and limitations in the MMTT should be considered. The range of conditions observed in MMTT test are shown in Figure F2-12 and are well within the range where fatigue damage is not expected to accumulate. However, as noted in Section F2-4, this design limit does not include the mean strain expected in HBU fuel rods. Further CIRFT testing is recommended to measure the potential effect of a prototypical mean strain, which is expected to be small compared to the gap between the observed strain amplitudes and the fatigue limit.

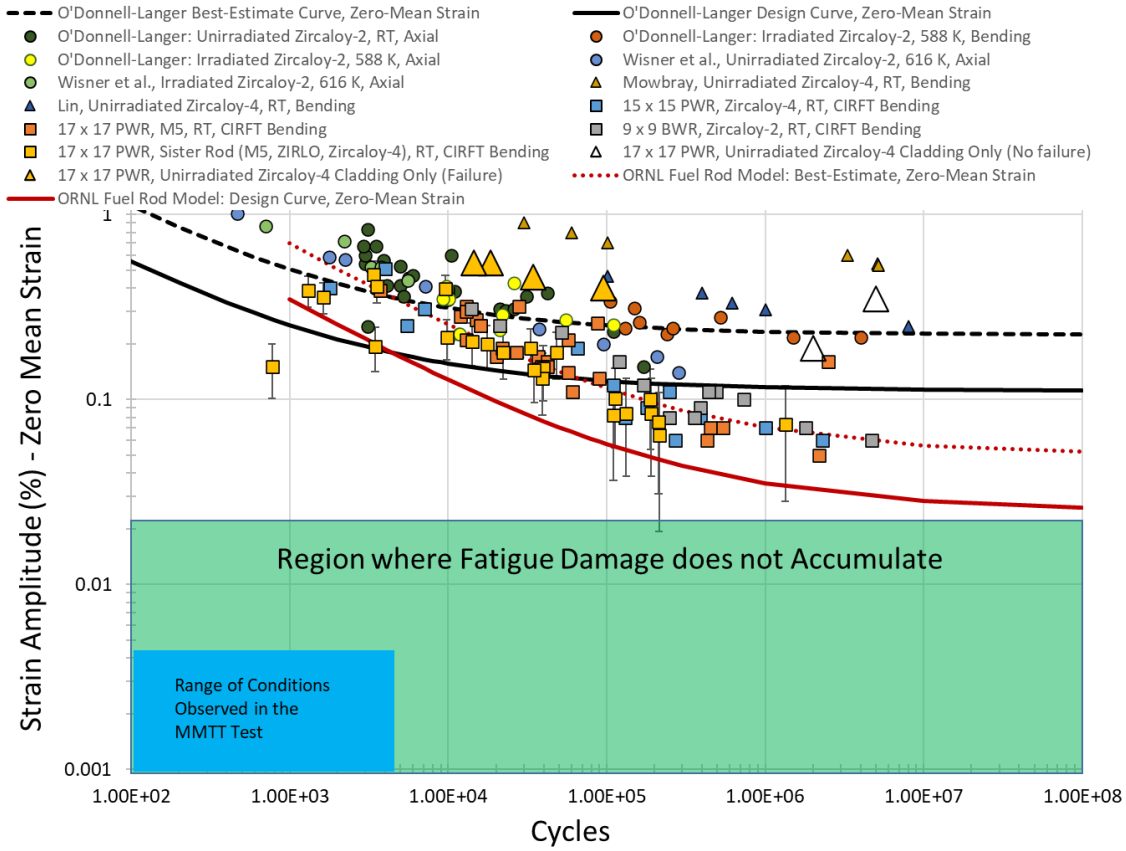

Figure F2-12. Comparison of the most sever range of conditions in the MMTT with the fatigue design curve for fuel rods tested under zero-mean strain conditions.

F2-8. Summary And Conclusions

In the fatigue evaluation of SNF under transportation conditions, the magnitude of the cyclic history is expected to be less than the fatigue limit of the fuel rods. Thus, to conclude that fatigue failures do not occur, it is sufficient to show that a strain amplitude representing an expected cyclic history is less than the fatigue limit of the SNF rods, which is also defined in terms of strain amplitude. The fatigue evaluation described in this paper considered the current available fatigue test data on cladding materials and HBU fuel rods, the potential non-conservatisms in the HBU fuel rod test data, and the measured cyclic data reported in the MMTT.

The fatigue limit of HBU fuel rods was degraded compared with the fatigue of cladding alloys. As discussed in other studies [F2-13]–[F2-18], cracks within the pellets and pellet-pellet interfaces are sources of stress/strain concentration, and these discontinuities in the pellet were concluded to be the cause of the observed degradation in fatigue performance. The magnitude of the stress/strain concentration can be estimated as the ratio of the fatigue limit for cladding alloys to that of the HBU fuel rods (0.2%/0.06% = 3.3).

Additionally, because there will be a nonzero-mean strain in SNF rods due to the RIP and bending under gravity, the fatigue limit based on testing performed at zero-mean strain is potentially non-conservative. The maximum axial cladding strain in SNF was predicted to range from ~0.02 to ~0.06%, depending on assumed burnup and temperature conditions. This range is comparable to the fatigue limit of HBU fuel rods, which is ~0.06% on a best-estimate basis and 0.03% on a design basis. Thus, strain due to mainly internal gas pressure is may further degrade the fatigue performance of SNF tested at zero-mean strain conditions, and it was estimated that a nonzero mean strain could degrade the fatigue limit further by ~7%. Additional fatigue testing of HBU fuel rods is recommended to determine the potential magnitude of the degradation in performance because of this nonzero-mean strain effect.

The effect of temperature on the fatigue limit of HBU fuel rods was also discussed. Although elevated temperature has been observed to decrease the fatigue limit of Zr alloys, the effect appears to be small. The authors concluded that fatigue testing of fuel rods at elevated temperature would be beneficial for determining whether there is a significant effect but that the conservatism in the fatigue design limit based on the RT test data alone likely covers any small degradation due to temperature. The main effect of temperature on the fuel rod is to increase RIP and thus the mean strain.

Finally, there is a significant gap between the maximum strain amplitude measured in the MMTT (0.0042%[4]) and the fatigue limit of the ORNL design curve for HBU fuel rods (~0.03%), indicating that fatigue damage is not expected during normal transportation conditions. However as noted above, additional fatigue testing is recommended to confirm that that fatigue limit at nonzero-mean strain does not decrease significantly.

[4] Note that only ~4000 cycles were observed in the range of 0.001% to 0.0042% [F2-31]

This page is intentionally blank

F2-9. REFERENCES

[F2-1] US NRC. 2020. *Standard Review Plan for Transportation Packages for Spent Fuel and Radioactive Materials.* NUREG-2216. Washington, DC: US Nuclear Regulatory Commission

[F2-2] W. J. O'Donnell and B. F. Langer. 1964. "Fatigue Design Basis for Zircaloy Components." *Nuclear Science and Engineering* 20, no. 1: 1–12.

[F2-3] M. Nakatsuka, T. Kubo, and Y. Hayashi. 1994. "Fatigue Behavior of Neutron Irradiated Zircaloy-2 Fuel Cladding Tubes." *Zirconium in the Nuclear Industry: Ninth International Symposium*, ASTM STP 1132, American Society for Testing and Materials, 230–245.

[F2-4] K. Snowden and P. Stathers. 1977. "The Fatigue Behavior of α-Zirconium and Zircaloy-2 in the Temperature Range of 20 to 700°C." *J. Nucl. Mater.* 67: 215–228.

[F2-5] S. Wisner, M. Reynolds, and R. Adamson. 1994. "Fatigue Behavior of Irradiated and Unirradiated Zircaloy and Zirconium." *Zirconium in the Nuclear Industry: Tenth International Symposium*. ASTM STP 1245, American Society for Testing and Materials, 499–520.

[F2-6] A. Soniak, S. Lansiart, J. Royer, J.-P. Mardon, and N. Waeckel. 1994. "Irradiation Effect on Fatigue Behavior of Zircaloy-4 Cladding Tubes." *Zirconium in the Nuclear Industry: Tenth International Symposium*, ASTM STP 1245, American Society for Testing and Materials, 549–558.

[F2-7] G. Brun, J. Pelchat, J. Floze, and M. Galimberti. 1987. "Cumulative Fatigue and Creep-Fatigue Damage at 350 °C on Recrystallized Zircaloy-4." *Zirconium in the Nuclear Industry: Seventh International Symposium*, ASTM STP 939, American Society for Testing and Materials, 597–616.

[F2-8] K. Pettersson. 1975. "Low-Cycle Fatigue Properties of Zircaloy-2 Cladding." *J. Nucl. Mater.* 56: 91–102.

[F2-9] D. Lee and P. Hill. 1976. "Effect of Oxygen on the Fatigue Behavior of Zircaloy." *J. Nucl. Mater.* 60: 227–230.

[F2-10] P. Pandarinathan and P. Vasudevan. 1980. "Low-Cycle Fatigue Studies on Nuclear Reactor Zircaloy-2 Fuel Tubes at Room Temperature, 300 and 350°C." *J. Nucl. Mater*. 91: 47–58.

[F2-11] X. Lin and G. Haicheng. 1999. "Low Cycle Fatigue Properties and Microscopic Deformation Structure of Zircaloy-4 in Recrystallized and Stress-Relieved Conditions." *J. Nucl. Mater*. 265: 213–217.

[F2-12] D. Mowbray. 1965. "Effects of 1.0% Superimposed Mean Strain on the Bending Fatigue Strength of Zircaloy-4." *Nuclear Applications* 1, no. 1: 39–48.

[F2-13] P. Cantonwine, R. Montgomery, J-A. Wang, H. Wang, B. Bevard, D. Skitt, Y. Sasikumar and O. Martinez. 2022. *Sister Rod Destructive Examinations (FY22) Appendix F: Cyclic Integrated Reversible Bending Fatigue Tests*. ORNL/TM-2022/2733. Oak Ridge: Oak Ridge National Laboratory.

[F2-14] H. Wang, J.-A. J. Wang, T. Tan, H. Jiang, T. S. Cox, R. L. Howard, B. B. Bevard, and M. E. Flanagan. 2013. "Development of U-Frame Bending System for Studying the Vibration Integrity of Spent Nuclear Fuel." *J. of Nuclear Materials* 440: 201–213.

[F2-15] J.-A. Wang and H. Wang. 2017. *Mechanical Fatigue Testing of High-Burnup Fuel for Transportation Applications*. NUREG/CR-7198, Rev. 1. Washington, DC: US Nuclear Regulatory Commission.

[F2-16] J.-A. Wang, H. Wang, H. Jiang, and B. Bevard. 2018. "High Burn-up Spent Nuclear Fuel Transport Reliability Investigation." *Nuclear Engr. and Design* 330: 497–515.

[F2-17] R. Montgomery, J-A. Wang, P. Cantonwine, Y. Sasikumar, H. Wang, B. Bevard, D. Skitt, and O. Martinez. 2021. *Sister Rod Destructive Examinations (FY21) Appendix F: Cyclic Integrated Reversible Bending Fatigue Tests*. ORNL/TM-2021/2291. Oak Ridge: Oak Ridge National Laboratory.

[F2-18] US NRC. 2020. *Dry Storage and Transportation of High Burnup Spent Nuclear Fuel*. NUREG-2224. Washington, DC: US Nuclear Regulatory Commission.

[F2-19] H. Jian, J.-A. Wang, and H. Wang. 2016. "The Impact of Interface Bonding Efficiency on High-Burnup Spent Nuclear Fuel Dynamic Performance." *Nuclear Engineering and Design* 309: 40–52.

[F2-20] E.A. Kalinina, C. Wright, L. Lujan, N. Gordon, S.J. Saltzstein, and K.M. Norman. 2018. *Data Analysis of ENSA/DOE Rail Cask Tests.* SAND2018-13258R. Sandia National Laboratory.

[F2-21] N. Klymyshyn, P. Ivanusa, K. Kadooka, C. Spitz, I. Ed, and P. R. Jensen. 2019. *Structural Dynamic Analysis of Spent Nuclear Fuel*. PNNL-29150, SFWD-SFWST-M2SF-19PN010202014. Richland: Pacific Northwest National Laboratory.

[F2-22] American Institute of Steel Construction. *Steel Construction Manual*. 14th edition. Table 3-23, Shears, Moments and Deflections.

[F2-23] R. Montgomery, R. N. Morris, R. Ilgner, B. Roach, J.-A. Wang, Z. Burns, J. T. Dixon, and S. M. Curlin. 2020. *Sister Rod Destructive Examination (FY20): Appendix B: Segmentation, Defueling, Metallographic Data and Total Cladding Hydrogen*. ORNL/SPR-2019/1251. Oak Ridge: Oak Ridge National Laboratory.

[F2-24] J.-A. Wang, H. Wang, B. B. Bevard, and J. M. Scaglione. 2017. *FY2017 Status Report: CIRFT Data Update and Data Analysis for Spent Fuel Vibration Reliability Study, Revision 1*. ORNL/SPR-2017/521. Oak Ridge: Oak Ridge National Laboratory.

[F2-25] G. M. O'Donnell and H. H. Scott. 2001. *A New Comparative Analysis of LWR Fuel Design*. NUREG-1754. US Nuclear Regulatory Commission.

[F2-26] J.-A. Wang, P. Cantonwine, Y. Sasikumar, H. Wang, B. Bevard, D. Skitt, and O. Martinez. 2022. *Sister Rod Destructive Examination (FY20): Appendix F: Cyclic Integrated Reversible-Bending Fatigue Tests*. ORNL/SPR-2021/2291. Oak Ridge: Oak Ridge National Laboratory.

[F2-27] J.-Y. Wang et al. 2018. "High Burnup Spent Nuclear Fuel Transport Reliability Investigation." *Nuclear Engineering and Design* 330: 497–515.

[F2-28] E. Schwenk et al. 1978. "Poisson's Ratio in Zircaloy-4 between 24° and 316°C." *J. Nucl. Mater.* 73: 129–131.

[F2-29] R. N. Morris and R. Montgomery. 2022. *Sister Rod Destructive Examination (FY20): Appendix C: Rod Internal Pressure, Void Volume, and Gas Transmission Tests*. ORNL/SPR-2020/1769. Oak Ridge: Oak Ridge National Laboratory.

[F2-30] R. Montgomery. 2021. *Sister Rod Destructive Examinations (FY21), Appendix G: CIRFT Uncertainty Calculations.* ORNL/SPR-2021/1840. Oak Ridge: Oak Ridge National Laboratory.

[F2-31] N. A. Klymynshyn, P. Ivanusa, K. Kadooka, C. Spitz, P. Jensen, S. Ross, B. Hanson, D. Garcia, J. Smith, and S. Lewis. 2018. *Modeling and Analysis of the ENSA/DOE Multimodal Transportation Campaign.* PNNL-28088. Richland: Pacific Northwest National Laboratory.

[F2-32] US NRC. 2007. *Standard Review Plan, Section 4.2 Fuel System Design, Revision 3*. NUREG-800. Washington, DC: US Nuclear Regulatory Commission.

[F2-33] R.W. Hertzberg. 1989. *Deformation and Fracture Mechanics of Engineering Materials*. Section 12.2.1. 3rd Edition John Wiley and Sons.

[F2-34] R.W. Shimskey et al. 2022. PNNL FY 2022 Sibling Pin Testing Results. M3SF-23PN010201043, PNNL-33781, Richland: Pacific Northwest National Laboratory.